SEM-EDS nanoanalysis of mineral composite materials: A Monte Carlo approach

SEM-EDS nanoanalysis of mineral composite materials: a Monte Carlo approach

Daniele Moro, Gianfranco Ulian, Giovanni Valdrè*

Centro di Ricerca Interdisciplinare di Biomineralogia, Cristallografia e Biomateriali, Dipartimento di Scienze Biologiche, Geologiche e Ambientali, Università di Bologna "Alma Mater Studiorum", Piazza P. San Donato 1 – 40126 Bologna, Italy

Abstract

A quantitative determination of chemical and mineral composition at the nanoscale is nowadays fundamental for the knowledge of properties of innovative composite materials. Scanning electron microscopy (SEM) equipped with energy dispersive X-ray spectrometry (EDS) is one of the most commonly employed spatially-resolved analytical methods, because of its versatility and great potential for nano-analysis. However, because of both complex architecture, texture and reduced grain sizes (micro-to-nano) in many composites, to avoid analytical errors, several effects related to electron and X-ray transport in solids must be considered. In the present work, a Monte Carlo SEM-EDS simulation approach is proposed and applied to selected micro-nanosized architectures usually found in composites. The effects of both micro-nanometric grain sizes (100 nm - 20 μm) and basic geometrical shapes (cubic, hemicylindrical) of embedded features in the sample matrix (a metal matrix and a glass fibre-reinforced cementitious composite), together with a realistic SEM-EDS setup, were studied. The results evidenced a high dependence of the simulated X-ray spectra versus particles thickness and shape, beam energy and sample-to-detector configuration, which directly affect a correct analytical characterization. The Monte Carlo simulation allowed to investigate and control the physical phenomena affecting the measurement and eventually to determine the optimal SEM-EDS parameters.

Keywords: SEM-EDS micro-nanoanalysis; Monte Carlo simulation strategy; nanocomposite materials; metal matrix composites; glass fibre-reinforced cementitious composites.

1. Introduction

Advances in research on structural materials, together with the need for environmentally friendly products for a suitably sustainable development drive the search and discovery of new materials, their production and delivery and/or the improvement of conventional ones. For instance, in the field of construction materials, ceramics, fly ash, steel slag, glass, metakaolin, fibres, plastics, sawdust, bamboo are some of the potential replacements investigated for conventional binders, aggregates and reinforcements [1].

Among the different classes of materials, composites are very interesting and promising because of the intrinsic great potential development (see for instance nanocomposites) and the wide variety of possible applications in various and different industrial fields, such as building construction, automotive, aerospace and health/medical. Research is addressed to improve both their features, *e.g.* strength, weight and durability, and production cost. In this regards, nanotechnology advances and the pronounced effects of tiny particles on the bulk properties promote this field as one of the most active in construction materials and civil engineering. In recent years, several types of nanoparticles have been incorporated into concrete, ceramic and polymeric materials, such as nano-TiO_2, nano-SiO_2, nano-metakaolin and carbon nanotubes, to develop innovative nanocomposites with unique and tailored physical and mechanical properties [2, 3].

A very interesting class of these materials is given by the ceramic matrix composites, where fibres can be incorporated in a ceramic matrix to improve its physical properties. To this aim, different kind of fibres were successfully employed: for instance, beside the early use of asbestos, nowadays steel and glass fibres, and newer types such as carbon, Kevlar, polypropylene, nylon fibres are used to

improve tensile and flexural strength, energy absorption capacity and toughness of concrete, with an always increasing research interest for structural applications. Recently, even natural fibres (e.g., cellulose, sisal, jute, flax, coir, bamboo, hemp) are evaluated as alternative to synthetic ones in fibre-reinforced concrete for the development of "environmentally friendly" construction materials, because they are lighter, cheaper and biodegradable [3-5]. The same scientific and applicative interest is also found in the development of fibre-reinforced geopolymer composites for structural applications. Also in this context, different inorganic or natural fibres are used to enhance the mechanical properties of the composite, such as fracture toughness and strength. Carbon, basalt or glass fibres are the most employed, but recently the use of alumina, silicon carbide or mullite is increasing [6].

Metal matrix composites (MMCs) represent another important class of composite materials, which are typically constituted by a rigid ceramic reinforcement in the ductile metal matrix, thus adding high strength, modulus and thermal stability to high ductility, toughness and machinability. The resulting high strength to weight ratio promotes the use of these composites as structural materials in the automotive, aerospace and sport industries. The most interesting MMCs are those where nanoparticles (and carbon nanotubes) are added as reinforcement, because, with respect to microparticles, they have a higher effect on the physical properties of the composite [2]. In this perspective, a significant research interest is driven towards the development of lighter structural metals (*e.g.*, Ti, Al, Mg) and Fe matrix composites with TiC or TiB_2 nanoparticulate [7].

From this brief introduction, it is clear that the investigation of the morphology, structure, chemistry, properties and applications of composite materials made of micro- and nanoparticles immersed in a matrix (*vide supra*), and of their interface, is a key interdisciplinary research for the development of novel materials. In this framework, both scanning electron microscopy (SEM) and transmission electron microscopy (TEM) play a fundamental role in their characterization. In particular, SEM is

widely employed to characterise nano-microstructures, to study the distribution of particles and/or fibres and to analyse the evolution of damage induced by strain [8-11].

SEM is also coupled with other techniques to provide further details on the composite material under investigation. For example, the electron backscatter diffraction (EBSD) allows studying the morphology and the local crystallographic texture of the sample, the size distribution of both particles and matrix grains and the distribution of misorientations [8, 9]. SEM allows also observing and characterising the presence of corrosion, its type, estimating its degree (depth) and the chemical nature of the corrosion products. By coupling scanning electron microscopy with energy dispersive X-ray spectroscopy (EDS), it is possible to study both the structure and the chemistry of the matrix-particle/fibre interfaces, whose properties influence the mechanical behaviour of the composite material. Indeed, the interface is of utmost importance because the transport of material between the components occurs across this boundary. Hence, to optimize both the mechanical and thermal properties of composites, one has to be able to control both the interfacial behaviour and the interphase. In this regard, SEM-EDS characterizations of the matrix-particle/fibre transition zone is fundamental and a key approach for this kind of studies [12, 13].

However, quantitative SEM-EDS X-ray microanalysis of particles and specimen features is challenging when they are in the micron domain and even more at the nanometre level. In fact, several effects may affect the quantitative X-ray microanalysis of micro- and nanometric particle/fibre features:

(i) the small thickness of the particle features with respect to the penetration depth of the electron beam;

(ii) the elastic and inelastic scattering of energetic electrons in the finite size (mass) of the particle features, which is greatly affected by the average atomic number;

(iii) the X-ray absorption path (influenced by both the particle shape and features), the fluorescence contribution and the take-off angle;

(iv) the configuration of the EDS detector with respect to the sample nano/microfeatures.

Under these conditions, it is not possible or advisable to adopt typical corrections for bulk matrix effects, *e.g.* ZAF iterative procedures, because these methods usually assume the specimen being flat and infinitely thick with respect to the electron beam penetration length. These assumptions, made for bulk samples, do not hold for micro- and nanoparticles [14]. Furthermore, it must be taken into account that the generation volume of secondary fluorescence could be more than an order of magnitude greater than the volume where the primary X-rays are generated by electron impact [15].

Because of the cited issues, it is advisable to develop suitable measurement strategies for the SEM-EDS X-ray microanalysis of this kind of composite materials. In this context, Monte Carlo simulation of electron transport and X-ray generation in solids under experimental conditions and/or in samples with complex geometry represents an invaluable tool. In fact, Monte Carlo simulation can help in both predicting systematic errors in SEM-EDS quantitative measurements of composite structures with micro- and nanotextures and particles, and devising analytical strategies to overcome them. All of the parameters determining the composite material (matrix, particles size, shape and orientation, texture) and the SEM-EDS instrumental configuration (*e.g.* electron beam energy, detector type, elevation angle and so on) have to be taken into account.

This work aims at showing the usefulness and effectiveness of SEM-EDS Monte Carlo simulation methods, presenting two different case studies in composite material research, namely (i) a metal matrix composite and (ii) a glass fibre-reinforced cement, each one characterized by different materials and particle shapes. Several SEM-EDS working conditions were considered in order to carefully understand their effect on the qualitative and quantitative microanalysis results and eventually provide a guide for precise and accurate measurements.

Furthermore, the reported Monte Carlo SEM-EDS strategy to solve the above two case studies is shown and explained in a fashion that can be applied to other composite materials investigated at the nanoscale.

2. SEM-EDS Monte Carlo theory and models

2.1. Theory and fundamentals

A precise and accurate SEM-EDS quantitative X-ray microanalysis of micro-to-nanosized structures, such as those characterizing composite materials, requires a deep understanding of the underlying physical phenomena, such as electron scattering in solids and related X-ray generation, absorption and fluorescence. Monte Carlo method to simulate electron transport is a powerful tool for investigating the various signals that are generated from the interaction of energetic electrons with matter [16, 17]. The Monte Carlo method allows to simulate the trajectories of electrons, X-rays generation and transport through the sample, and to a realistic EDS detector to generate simulated X-ray spectra. Here, each 3D electron trajectory is constituted by a series of straight segments, whose length depends on the mean free path of the electron. Each segment ends when an elastic scattering event occurs. After each scattering event, the electron energy is decreased to model an average energy loss as the result of inelastic collisions (continuous slowing down approximation) [18]. The elastic scattering is modelled by using the Mott cross section of Jablonski and co-workers [19], the Mott scattering cross section of Czyzewski and co-workers [20] and a basic screened Rutherford model [21]. The energy loss *dE* with the travelled distance *ds* (keV/cm) is modelled with the Joy-Luo expression [22], an empirical modification of the Bethe equation of the energy loss [23]:

$$\frac{dE}{ds} = -7.85 \times 10^4 \frac{Z\rho}{AE_i} \ln\left(\frac{1.166E_i}{J^*}\right)$$

$$J^* = \frac{J}{1 + (kJ/E)}$$

$$k = 0.731 + 0.0688 \log_{10} Z$$

$$J = (9.76Z + 58.5Z^{-0.19}) \times 10^{-3}$$

where A is the atomic weight (g/mole), E_i is the electron energy (keV) at any point in the specimen, Z is the atomic number, ρ is the density (g/cm^3), J is the average loss in energy per event and J^* is the modified mean ionization potential.

The ionisation cross-section, σ_i, is modelled using the parameterized analytical expression of Bote and Salvat [24, 25]:

for $U \leq 16$, $\sigma_i = 4\pi a_0^2 \frac{U-1}{U^2}\left(a_1 + a_2 U + \frac{a_3}{1+U} + \frac{a_4}{(1+U)^3} + \frac{a_5}{(1+U)^5}\right)^2$

for $U \geq 16$, $\sigma_i = \frac{U}{U+b} 4\pi a_0^2 \frac{A_i}{\beta^2}\left\{[\ln X^2 - \beta^2](1 + g_1 X^{-1}) + g_2 + g_3(1-\beta^2)^{1/4} + g_4 X^{-1}\right\}$

where $U = E/E_c$ is the overvoltage of electrons with kinetic energy E for ionization of a particular shell with critical ionization energy E_c, a_0 is the Bohr radius, a_1, a_2, a_3, a_4, a_5, b, g_1, g_2, g_3, g_4 are parameters characteristic of each element and electron shell, $A_i = \alpha^2 M_j^2/2$ with α fine-structure constant and M_j^2 squared dipole-matrix element for ionization, $\beta = v/c$ with v electron velocity and c speed of light, $X \equiv p/(m_e c)$ with p electron momentum and m_e electron mass.

The core-shell vacancy relaxation process for the generation of characteristic X-rays, assumed isotropic and not taking into account photon polarization, is modelled using the fluorescence yields tabulated by Perkins and co-workers [26]. Primary continuum (Bremsstrahlung) emission, assumed not isotropic, is modelled using Seltzer and Berger's tabulated partial and total cross-sections for Bremsstrahlung production [27-30]. The mass absorption coefficients for X-ray absorption are the photoelectric component of those calculated by Chantler and co-workers [31].

The primary X-ray photons (Bremsstrahlung and characteristic) are propagated from the generation point in a random direction. After a computed mean free path for photoionization, they are absorbed by photoionization or escape the materials. Hence, the photoionization event is followed by relaxation with the generation of the characteristic X-rays (i.e., secondary X-ray fluorescence) of the absorbing element, according to the associated probabilities [15].

2.2. Composite material models

The first simulated model is a Fe–titanium diboride (TiB_2) composite. It is a new type of metal matrix composite, made of a full ferritic matrix (α-Fe, body-centred cubic crystallographic structure) and ceramic micro-to-nano-particles of TiB_2 (hexagonal compact crystallographic structure) [32]. This new composite is attractive for automotive and aerospace industrial applications due to the very high elastic moduli and low density of TiB_2 particles, leading to an overall increase in the specific stiffness. In this regard, the influence of the microstructural features on the macroscopic mechanical behaviour of crystalline materials is the subject of many studies, and it is of paramount importance to investigate the structure and chemistry of the composite constituents, their interfaces and the damage mechanisms of Fe–TiB_2 [32, 33]. In this case, to clearly show the above reported possible effects on SEM-EDS X-ray microanalysis, a simple Monte Carlo model was considered, geometrically consisting of a cubic-shaped TiB_2 ceramic particle (with a side of 500 nm) placed above an "infinitely" extended iron substrate as shown in Fig. 1a. Mass density of 4.5 g/cm^3 [34] and 7.87 g/cm^3 [35] were used for the TiB_2 nanoparticle and Fe matrix, respectively. The energy of the electron beam was varied between 1 and 25 keV, with a step of 1 keV, to study its effect on the analysis and identify the optimal working conditions.

The second simulated model is a glass fibre-reinforced cement. The study of glass fibre-reinforced cement/concrete as a structural material is promoted by the effect of the fibres in the cementitious matrix, which leads to an increase in the tension and impact strength of the material, and light-weight characteristics relatively to unreinforced Portland cement [36, 37]. A glass fibre is an amorphous material characterized by very high tensile strength, suitable elasticity, good thermal performance, excellent water resistance, good electrical and thermal insulation, good sound insulation and ability to resist shrinkage. An alkali-resistant (AR) ZrO_2-glass fibre is required in a cement matrix, to avoid erosion caused by a highly alkaline environment, improving the chemical stability. Standard AR-glass contains about 16–20 wt.% zirconium dioxide and provides therefore a significantly enhanced

resistance in highly alkaline environments, as compared to conventional glasses. SEM-EDS qualitative and quantitative microanalysis is used to investigate the nominal composition of the glass fibre, fibre–matrix interface, the chemical interaction of glass fibres in concrete mixtures, evaluating corrosion phenomena in order to improve the durability of glass fibre reinforced cement composites and minimize the degradation of mechanical properties [38-40]. In this regard, the second simulated model is a hemicylindrical alkali-resistant glass fibre embedded in a quartz (SiO_2) matrix, infinitely thick with respect to the electron penetration depth, thus simulating a case study of a fibre-reinforced ceramic matrix sectioned for SEM-EDS microanalysis (Fig. 1b). A typical composition of AR glass fibre was considered as reported in Table 1, with mass density 2.70 g/cm^3 [41-43]. The density of the quartz matrix was set to 2.65 g/cm^3, corresponding to α-quartz, hexagonal crystal system [35].

Table 1. Oxides mass fraction (weighted percentage) of alkali-resistant glass fibre.

SiO_2	ZrO_2	Na_2O	TiO_2	K_2O	Al_2O_3
62	18	14	3	2	1

In our Monte Carlo simulation, the fibre radius (coinciding with the hemicylinder thickness in our model) was varied to 0.1, 0.3, 0.5, 0.7, 1, 3, 5, 7, 10 and 20 μm with constant fibre length of 50 μm, whereas the energy of the electron beam to 5, 10, 15, 20 and 25 keV. To investigate the effect of the sample-to-detector orientation two configurations were considered: the fibre long axis oriented perpendicularly to the fibre-to-detector direction (case A in Fig. 1b), and the fibre long axis parallel to the fibre-to-detector direction (case B in Fig. 1b). In both cases, the beam (5 nm in diameter, zero divergence) was placed on the centre of the fibre. Finally, to investigate the effect of the beam position with respect to the fibre and the matrix on the microchemical analysis, we performed several simulations by varying the beam focusing point starting from the glass fibre edge (fibre-matrix interface) and moving towards the quartz matrix, *i.e.* away from the fibre. In this case, we considered only the detector configuration labelled as A in Fig.1b.

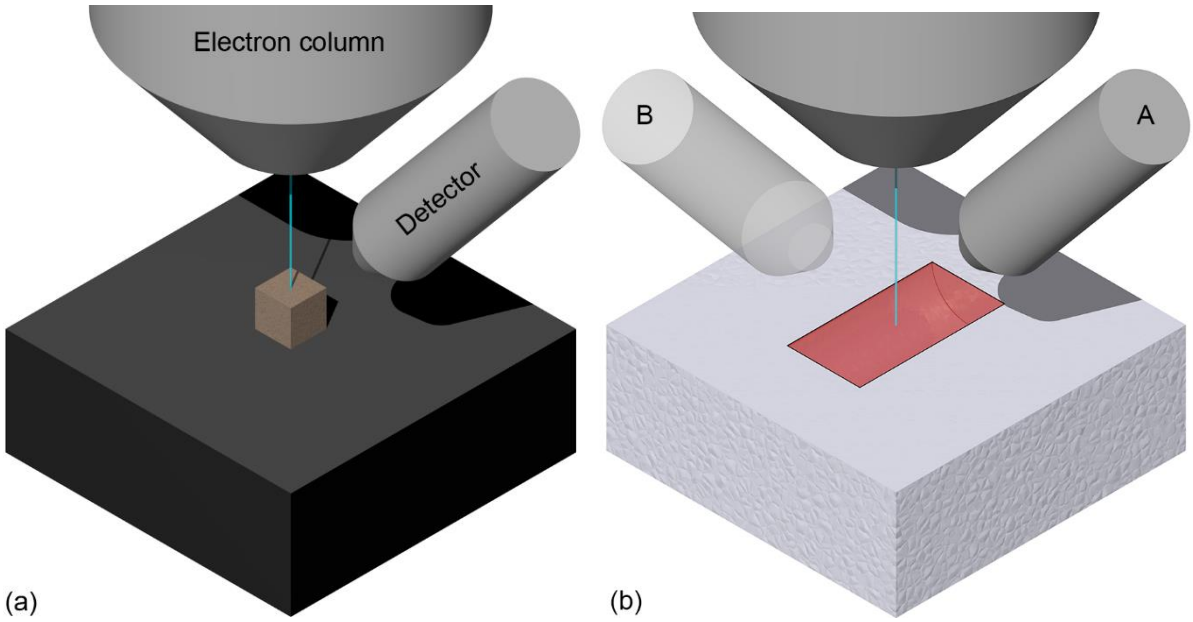

Fig. 1. Representative geometrical models of the simulated configurations. (a) Titanium diborate cubic-shaped nanoparticle placed above a pure iron substrate, with the electron beam focussed on the top of the nanoparticle in a centred position and the Si(Li) EDS detector with an elevation angle of 40°. (b) Section of an alkali-resistant glass fibre embedded in a quartz matrix with the electron beam focussed in the middle of the fibre, with the fibre long axis perpendicularly oriented with respect to the detector (configuration A) or the fibre long axis oriented towards the detector (configuration B). Images were realized with the POV-Ray 3D imaging software with shadows of the detector and objective lens onto the substrate surface and illuminating light up front left.

2.3. SEM-EDS configuration

For both simulations, the SEM-EDS set-up was modelled considering realistic devices and measurement conditions. The electron source was modelled with a Gaussian profile (Gaussian width of 5 nm) and focussed in parallel illumination (beam divergence zero) onto the analytical point. A realistic Si(Li) energy dispersive X-ray detector was modelled, accounting for detector efficiency and resolution: Moxtek AP 3.3 ultrathin polymer window, a detector area of 10 mm^2, a 7 nm gold layer, a 10 nm dead layer, a 3 mm thick detector diode, 4096 channels each of 10 eV, with a resolution of 130 eV (FWHM at Mn Kα). The sample-to-detector distance was set to 45 mm, the detector elevation

angle to 40° and the azimuthal angle was varied depending on the specific simulation, as reported in the proper sections.

3. Results and Discussion

SEM-EDS quantitative X-ray microanalysis of nano to microsized features, for which the assumptions typically considered for bulk samples do not apply, is often a challenge. In the present simulations, we defined as "bulk material" a substrate whose thickness is much greater than the electron penetration depth, i.e. a material where all electrons trajectories and generated X-rays are inside. If the scattering volume of the electrons is comparable or greater than the size of the object under analysis and/or if shape factors further contribute to the deviation from the behaviour of a bulk material, the interaction of electrons or X-rays with surrounding materials can lead to substantial errors in the quantification. Monte Carlo simulation is a valuable theoretical analytical tool for the comprehension of complex physical phenomena that can occur in the quantitative X-ray microanalysis of nano/microsized particles and samples with complex geometries.

As explained in the previous chapter, here we present the results and predictions of Monte Carlo simulations, and consequent indications for a precise ad accurate microanalysis, on two particular cases of composite materials, with realistic experimental conditions:

i) A metal matrix composite model, constituted by a cubic-shaped TiB_2 ceramic nanoparticle above a ferritic matrix;
ii) A glass fibre-reinforced cementitious composite model, consisting of an alkali-resistant hemicylindrical glass fibre embedded in a quartz matrix, taking into account:
    (1) Glass fibre analysis, changing the fibre-to-detector relative orientation;
    (2) Matrix – fibre interface analysis, focussing the beam on the matrix varying its position relatively to the fibre edge.

3.1. Metal matrix composite

The first model implemented to show the powerfulness of the SEM-EDS Monte Carlo strategy for the nanoanalysis of composite materials is a metal matrix nanocomposite. To this regard, a simple geometry was chosen to model a cubic-shaped ceramic nanoparticle of titanium diboride onto a pure iron substrate (Fig. 1a), as detailed in Section 2. The side of the TiB_2 cubic nanoparticle was fixed to 500 nm, the electron beam was focussed on the top of the particle in a centred position, and the effects on the microanalysis of different beam energies was investigated varying the energy between 1 and 25 keV, with a 1 keV step. The simulations took into account also secondary fluorescence generation and transport from Bremmstrahlung and primary characteristic X-rays. The simulated X-ray spectra were background subtracted and the characteristic peaks were integrated. Fig. 2a reports with a blue line (circular marker) the trend of the integrated intensity for the case of Ti Kα X-ray line (4.508 keV) as a function of the beam energy, whereas an orange line (square marker) shows the trend of the same X-ray line in the case of a bulk material. It should be considered and pointed out that although the presented SEM-EDS Monte Carlo strategy has a general validity and applicability, these results are specifically related to the particular SEM-EDS configuration and type of detector here simulated. It is worth noting that at 5 keV, even if the energy is sufficient to generate the Ti Kα X-ray line, the signal-to-noise ratio may be extremely low and the line could not be easily discernable. Increasing the beam energy, the Ti Kα integrated intensity calculated for the TiB_2 particle follows the "bulk" trend until approximately 10 keV. For higher energies a strong deviation of the X-rays from the TiB_2 particle with respect to the bulk material is observed. The cited deviation is also plotted in Fig. 2b, which reports the trend of the k-ratio, defined as the ratio between the integrated intensity calculated for the nanoparticle and the integrated intensity calculated for the bulk material, for Ti Kα versus the electron beam energy in this specific configuration. Thus, a k-ratio deviating from the unit (i.e., the

bulk) is indicative of a quantitative underestimation (if lower than unity) or overestimation (if k-ratio > 1) for the specific element considered. The k-ratio curve suggests 8 keV as optimal working energy because it is a compromise between the necessity of high X-ray counts (for statistical mean) and the minimization of the deviation from the bulk counts. In this case, Monte Carlo simulation allows to define the optimal experimental SEM-EDS configuration and parameters.

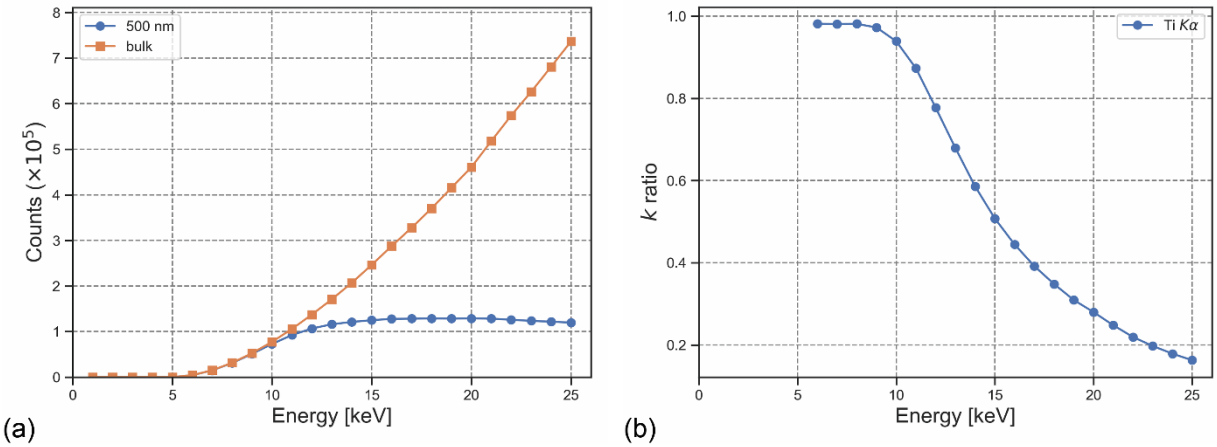

Fig. 2. (a) Simulated trend of the integrated X-ray intensity of Ti Kα line versus electron beam energy for a 500 nm thick, cubic-shaped TiB_2 nanoparticle (blue line, circular marker) and a bulk TiB_2 material (orange line, square marker). (b) Trend of the k-ratio calculated from the data in (a) as a function of incident beam energy.

The cause of this particular trend has to be interpreted considering the complex physical phenomena involving elastic/inelastic scattering of electrons inside the particle and substrate, X-ray generation, transport and absorption, together with the particle thickness and shape components. To clear these points, Fig. 3a shows the electron scattering inside the TiB_2 particle and Fe substrate in the case of a 25 keV electron beam. The electrons pass through the TiB_2 nanoparticle (green trajectories) penetrating and scattering also into the substrate (blue trajectories) for several micrometres. The finite lateral size of the nanoparticle with respect to the electron scattering path allows electrons scattering also out of the particle sides. The grey trajectories are related to backscattered (BS) electrons. Thus,

electrons do not only excite X-ray generation from titanium diborate, but also from the iron substrate. In addition, in this SEM configuration, the backscattered electron resolution is quite poor, as many BS electrons come from the substrate. In order to optimize X-ray generation from the nanoparticle, in this specific case and configuration, a beam energy of 8 keV should be preferred respect 25 keV. At this energy value, 8 keV, electrons and X-ray generation are mainly confined inside the nanoparticle, as clearly shown in Fig. 3b. Note also that almost all high-angle backscattered electrons come from the surface of the TiB_2 particle.

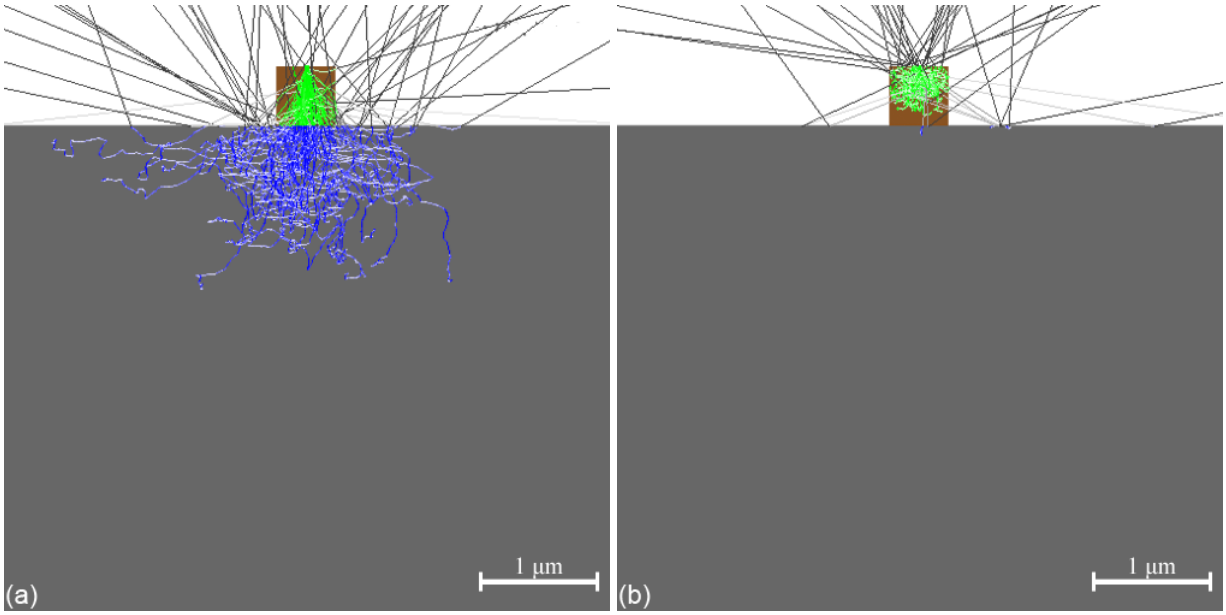

Fig. 3. 2D projection of simulated 3D electron trajectories inside a cubic-shaped TiB_2 nanoparticle (brown cube, 500 nm thick, and green trajectories) and underneath pure iron substrate (grey area and blue trajectories), for a 25 keV (a) and 8 keV (b) electron beam focussed on the top of the particle in a centred position. See the text for details.

3.2. Glass fibre-reinforced cementitious composite

A second 3D model was implemented to show other very useful characteristics and applications of the proposed SEM-EDS Monte Carlo strategy for the nanoanalysis of composite materials. An alkali-resistant hemicylindrical glass fibre, with composition reported in Section 2, embedded in a quartz

matrix was chosen as an example to simulate a section of a glass fibre-reinforced cementitious composite prepared for SEM-EDS analysis (see Fig. 1b). Usually, composite specimen for SEM-EDS analyses are embedded in resin and polished, and the model here reported represents the typical features of a polished fibre into a SiO_2 matrix, as shown in Fig. 1b. In this model, the radius of the fibre represents its thickness, and various effects on the microanalysis were modelled: (i) the thickness effect; (ii) the beam energy effect and (iii) the sample-to-detector orientation for the analysis of the fibre, and (iv) the electron beam position with respect to the fibre edge (matrix-fibre interface) for the analysis of the matrix.

3.2.1. Glass fibre analysis

Here, the electron beam was focussed on the top of the hemicylindrical fibre in a centred position. Fig. 4 reports as an example a 2D view (x,z section plane) of a fibre with a radius of 700 nm (coloured in red) embedded in the quartz matrix (coloured in light grey), together with the 2D projection of the 3D electron trajectories. Fig. 4a shows the trajectories of 25 keV incident electrons that penetrate through the fibre with low lateral scattering inside the fibre (green trajectories), entering the quartz matrix (blue trajectories) for more than 4 micrometres in depth and laterally scattering about 4 micrometres apart from the focus point. Grey trajectories are related to backscattered electrons both from the fibre and the matrix. The use of a 10 keV electron beam greatly reduces the electrons scattering volume that is mainly confined inside the fibre (green lines), but still some electrons (blue lines) enter the SiO_2 matrix for 100-200 nm (Fig. 4b). With a 5 keV electron beam the electron scattering volume is completely confined inside the fibre (green lines), but at the surface and with a great reduction of the X-ray intensity detection (see Fig. 5). After a detailed analysis, we found that with a 8 keV electron beam we have the optimization of both the electron penetration depth and X-ray detected signal as shown in Fig. 4d.

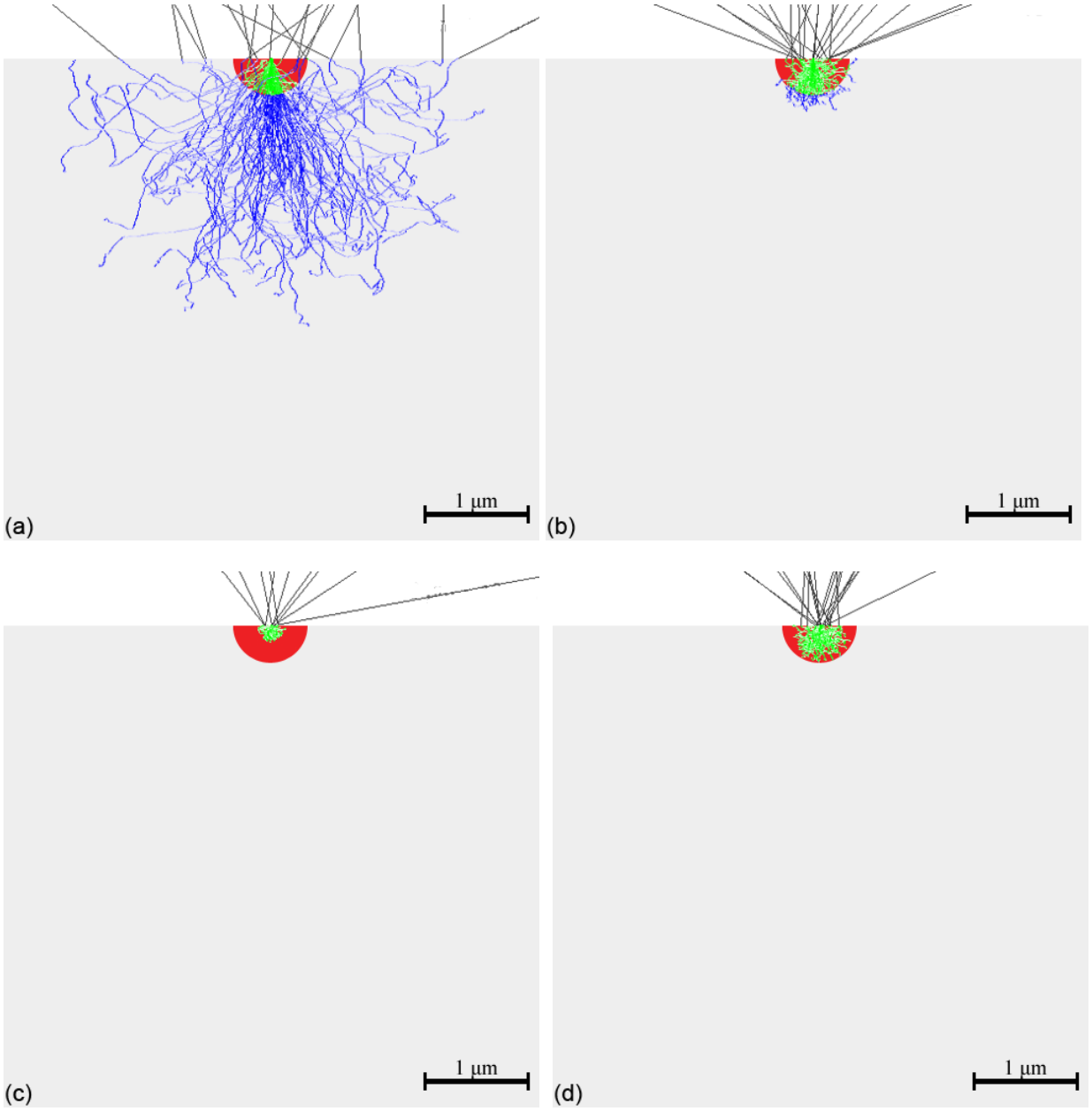

Fig. 4. Simulation of electron trajectories inside an alkali-resistant glass fibre with a radius of 700 nm (red area, green trajectories) and the embedding quartz matrix (light grey area, blue trajectories) for a 25 keV (Fig. 4a), 10 keV (Fig. 4b), 5 keV (Fig. 4c) and 8 keV (Fig. 4d) electron beam energy. The images represent a 2D section of a 3D geometrical model, with 2D projection of 3D electron trajectories. The grey lines represent the backscattered electron trajectories.

Many simulations were carried out with a fibre radius ranging between 100 nm and 20 µm, an electron beam energy of 5, 10, 15, 20 and 25 keV, and the fibre long axis placed perpendicularly to the detector

orientation (case A in Fig. 1b). Generally, the integrated X-ray intensity as a function of the fibre radius presented a marked non-linear reduction in the case of Zr L (Lα + Lβ), Al Kα, K Kα, K Kβ, Na Kα, Ti Kα, Ti Kβ and an increase for Si Kα and O Kα (due to the contribution of the quartz matrix), with a specific trend dependent on the type of X-ray emission line considered and particular beam energy. The intensity variation occurs when the X-ray generation path is greater than the radius of the hemicylindrical fibre and started from fibre thickness (radius) less than 5 μm at 25 keV, 3 μm at 20 keV and 15 keV, 1 μm at 10 keV and 0.2 μm at 5 keV. Fig. 5 reports the case of Si Kα (a, c) and Zr L (b, d). As clearly visualized in the graph of the Si Kα k-ratio (Fig. 5c), the intensity of Si is largely overestimated for the smaller radius values, with the calculated k-ratio at 25 keV and 100 nm radius higher than the bulk reference value (i.e., 1.0) of about 70%, because of the excitation of silicon belonging to the quartz matrix. An opposite trend is observed for Zr L k-ratio (Fig. 5d), with values calculated at 25 keV and 100 nm radius that were less than 3% of the bulk ones. As a practical example, in a quality control assessment during industrial production of this kind of glass fibre-reinforced composite, optimized SEM-EDS parameters are mandatory to avoid microchemical misinterpretations of correctly manufactured specimens, or vice versa.

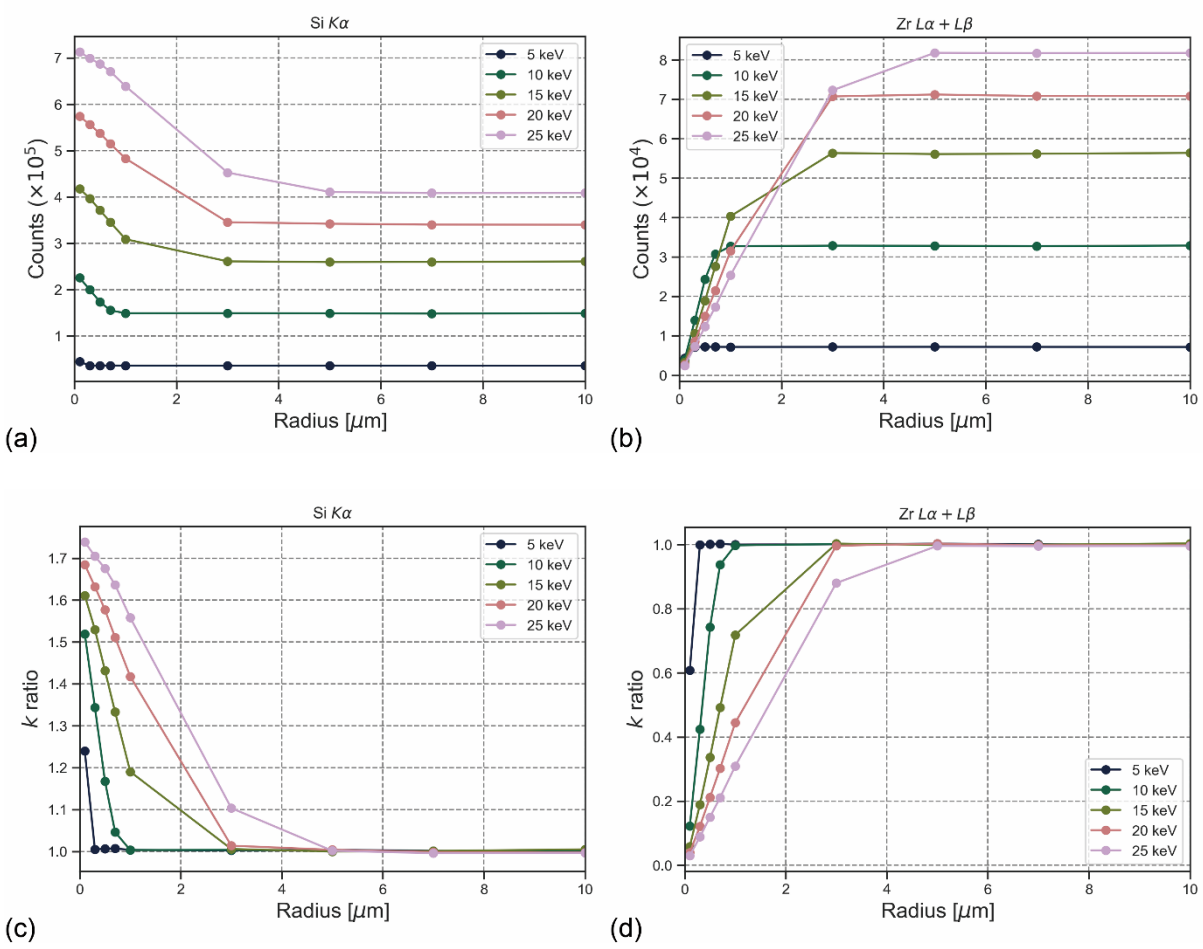

Fig. 5. Integrated X-ray intensity (a, b) and respective k-ratio (c, d) for Si Kα and Zr L for a hemicylindrical alkali-resistant glass fibre embedded in a SiO_2 quartz matrix, as a function of fibre radius and beam energy, in the case of a 90° fibre-to-detector orientation (case A in Fig.1b). The k-ratio is defined as the ratio of the X-ray intensity measured for the sample and that of a reference bulk material.

The same approach was employed to assess the effect of the fibre-to-detector orientation on the quantitative SEM-EDS evaluation. To this aim, a further model was developed with the fibre long axis oriented towards the detector (Fig. 1b, case B). The simulation results showed that k-ratios are closer to 1 (i.e., bulk material behaviour) in the case B, thus indicating this configuration as the preferred one for the quantitative microanalysis of the glass fibre. The percentage differences between the k-ratios obtained for the two configurations (cases A and B in Fig. 1b), namely the variations related to the different sample-to-detector orientation, were up to 7% for O Kα, less than 3% for Si

Kα, less than 2% for the other elements (Zr L, Na Kα, Al Kα, Ti Kα and K Kα), calculated as $(k_A - k_B)/k_B$, where k_A and k_B are the k-ratios for the case A and case B, respectively.

3.2.2. Matrix – fibre interface analysis

In the field of nano and microcomposite materials, the understanding of the chemical composition, the structure and the features of the interface between different components is of paramount importance. However, in this case when using SEM-EDS X-ray microanalysis it is fundamental to understand the limits and the potential of the SEM-EDS methodology by accurately considering the underlying physical phenomena. In fact, while the spatial resolution of the secondary electrons can reach the nanometre level, the chemical spatial resolution is much lower, thus particular care has to be paid when selecting the spot for the microanalysis to avoid quantification errors. Here, as an example, we investigated the SEM-EDS analytical measurement of the quartz matrix-fibre interface, by focussing the electron beam onto the quartz matrix at arbitrarily chosen distances from the fibre edge, as shown in the model of Fig. 6. The simulation was performed with an electron beam energy set to 15 keV and the distance of the focussing point from the fibre edge was varied between 100 nm and 100 μm. The fibre radius (which coincides with the hemifibre thickness in our model) was set to 500 nm.

At distances less than 2 μm from the edge, a significant contribution from the fibre X-ray emission line of Na Kα (Fig. 7a) was observed in the simulated EDS spectra, whereas Zr Lα+Lβ (Fig. 7b) is still not significant at 1 μm. Consequently, even the X-ray emission from elements of the quartz matrix, Si Kα (Fig. 7c) and O Kα (Fig. 7d) are affected, with a non-linear decrease of the intensity. This led to a loss up to about 3% and 13% of the integrated X-ray intensity for Si Kα and O Kα, respectively, at a distance of 100 nm from the fibre edge. This specific trend is affected by the X-rays absorption from the fibre elements, electron scattering inside the fibre, the particular fibre geometry and the positions of the beam focussing point and detector.

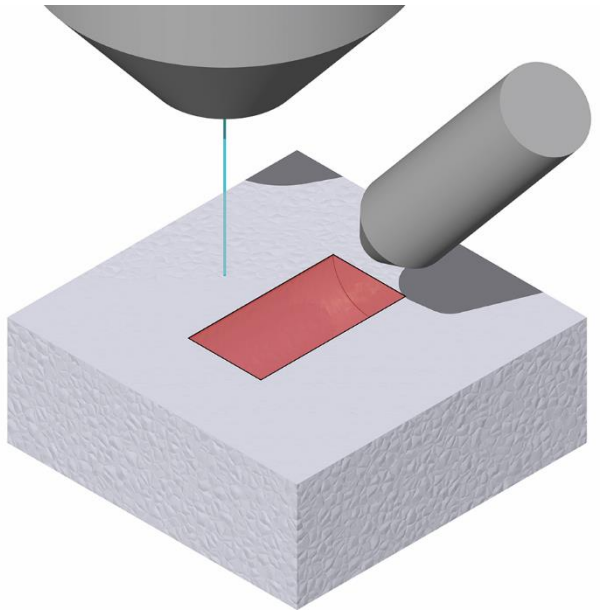

Fig. 6. Representative geometrical model of the configuration employed for the matrix - fibre interface analysis. A section of an alkali-resistant glass fibre is embedded in a quartz matrix with the electron beam focussed on the quartz matrix at an arbitrarily chosen distance from fibre edge. The scheme was realized with the POV-Ray 3D imaging software with shadows of the detector and objective lens onto the substrate surface and illuminating light up front left.

Concluding, in this particular case here considered (15 keV), it is advisable to perform the microanalysis of the matrix by focussing the electron beam not closer than about 10 μm from the fibre edge. However, the results allow us to draw some other important considerations that can be applied in other analytical circumstances. The specimen features could play an important role. For example, the glass fibres could be not straight as in the presented model, but twisted and/or tangled. Similar considerations could be extended to the analysis of the glass fibre.

In general, the SEM-EDS analytical strategy must be devised according to the specimen under investigation, with its peculiar chemistry, features and geometry (shapes and thicknesses). The present Monte Carlo simulations are just some case studies that showed how this approach can be

employed to optimize the experimental SEM-EDS setups and parameters for accurate chemical analyses.

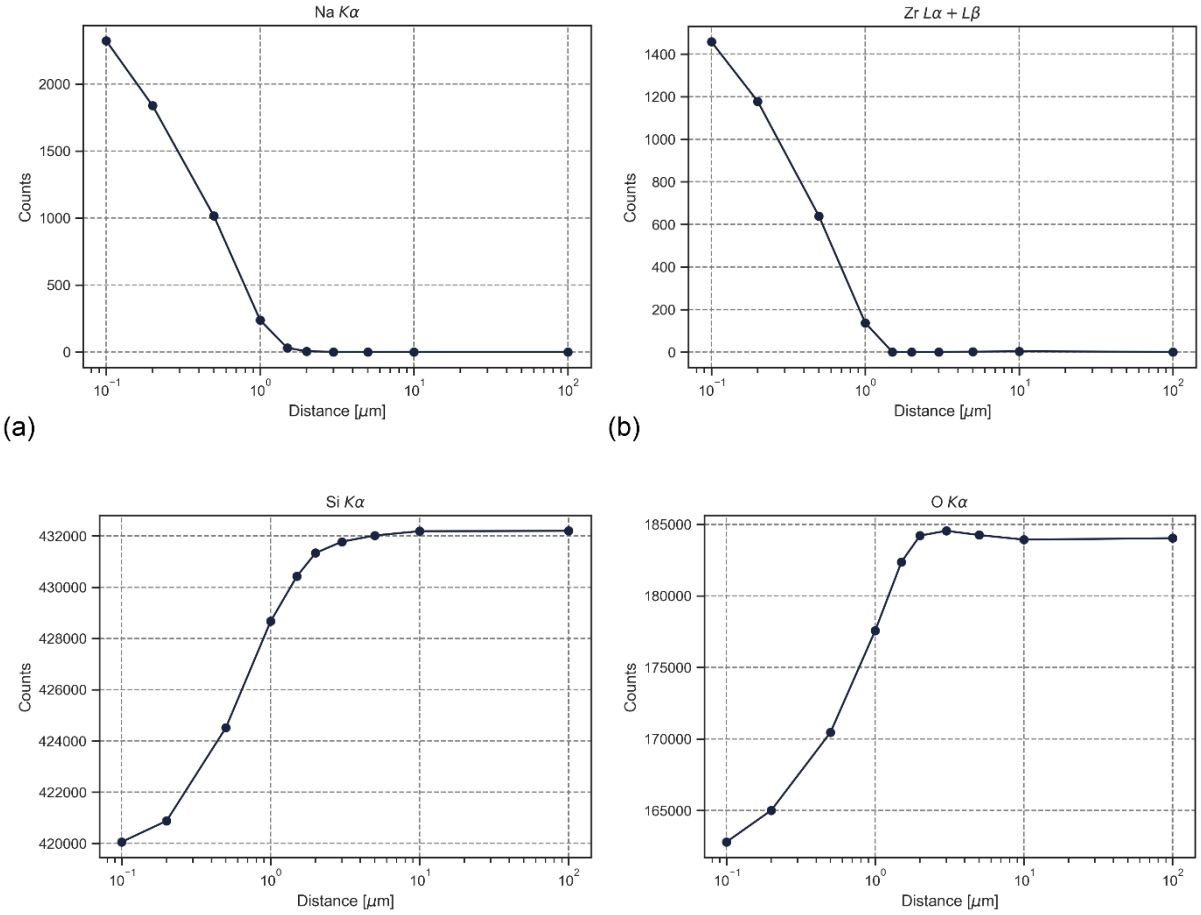

Fig. 7. Integrated X-ray intensity calculated from simulated EDS spectra of the quartz matrix as a function of the distance of the analytical point from the glass fibre edge. (a) Trend of Na Kα X-ray emission line, from the fibre. (b) Trend of Zr L X-ray emission line, from the fibre. (c) Trend of Si Kα X-ray emission line. (d) Trend of O Kα X-ray emission line.

4. Conclusion

In the field of characterization and development of micro-nanocomposites, scanning electron microscopy with energy dispersive X-ray microanalysis is a fundamental methodology for the

understanding of nanomorphology and nanostructure in relation to chemical composition and transformation products. However, as shown and discussed in detail within the results of the presented study, SEM-EDS micro-nanoanalytical capability applied to the study of nanocomposites could be subject to qualitative and quantitative analytical errors (several percentages in the simulated models), if the experiment is not properly designed for the kind of composite under investigation. The Monte Carlo SEM-EDS method, here employed and shown for two particular kinds of composite with peculiar shapes of the embedded nanoparticles, allows investigating the physical phenomena that could affect the measurement, hence determining the optimal SEM-EDS instrumental parameters and sample arrangement for precise and accurate quantitative analysis. The presented approach is intended to be a guide to the microanalysis of various and different types of micro- and nanocomposites, aiding the development of specific, correct and optimized analytical strategies.

References

[1] Anandaraj S, Rooby J, Awoyera PO, Gobinath R. Structural distress in glass fibre-reinforced concrete under loading and exposure to aggressive environments. Construction and Building Materials. 2019;197:862-70.

[2] Haghi AK, Oluwafemi OS, Maria HJ, Jose JP. Composites and Nanocomposites. Oakville, Canada: Apple Academic Press, 2013.

[3] Low IM. Advances in Ceramic Matrix Composites. Second ed. Duxford, UK: Elsevier, 2018.

[4] Brandt AM. Fibre reinforced cement-based (FRC) composites after over 40 years of development in building and civil engineering. Composite Structures. 2008;86:3-9.

[5] Bentur A, Mindess S. Fibre Reinforced Cementitious Composites. Second ed. London, UK: Taylor & Francis, 2007.

[6] Lin T, Jia D, He P, Wang M. In situ crack growth observation and fracture behavior of short carbon fiber reinforced geopolymer matrix composites. Materials Science and Engineering A. 2010;527:2404-7.

[7] Hadjem-Hamouche Z, Chevalier JP, Cui Y, Bonnet F. Deformation behavior and damage evaluation in a new titanium diboride (TiB_2) steel-based composite. Steel Research International. 2012;83:538-45.

[8] Dammak M, Gaspérini M, Barbier D. Microstructural evolution of iron based metal-matrix composites submitted to simple shear. Materials Science and Engineering A. 2014;616:123-31.
[9] Gaspérini M, Dammak M, Franciosi P. Stress estimates for particle damage in Fe-TiB_2 metal matrix composites from experimental data and simulation. European Journal of Mechanics, A/Solids. 2017;64:85-98.
[10] Moro D, Valdrè G. Effect of shape and thickness of asbestos bundles and fibres on EDS microanalysis: a Monte Carlo simulation. 14th European Workshop on Modern Developments and Applications in Microbeam Analysis (Emas 2015 Workshop). 2016;109.
[11] Valdrè G, Moro D, Ulian G. Monte Carlo simulation of the effect of shape and thickness on SEM-EDS microanalysis of asbestos fibres and bundles: The case of anthophyllite, tremolite and actinolite. IOP Conf Ser Mater Sci Eng. 2018;304:012019.
[12] Kwan WH, Cheah CB, Ramli M, Chang KY. Alkali-resistant glass fiber reinforced high strength concrete in simulated aggressive environment. Materiales de Construccion. 2018;68.
[13] Yilmaz VT, Glasser FP. Reaction of alkali-resistant glass fibres with cement. Part 1. Review, assessment, and microscopy. Glass Technology. 1991;32:91-8.
[14] Ritchie NWM. Using DTSA-II to Simulate and Interpret Energy Dispersive Spectra from Particles. Microscopy and Microanalysis. 2010;16:248-58.
[15] Ritchie NWM. Efficient Simulation of Secondary Fluorescence Via NIST DTSA-II Monte Carlo. Microscopy and Microanalysis. 2017;23:618-33.
[16] Moro D, Ulian G, Valdre G. SEM-EDS microanalysis of ultrathin glass and metal fragments: measurement strategy by Monte Carlo simulation in cultural heritage and archaeology. International Journal of Conservation Science. 2020;11:223-32.
[17] Moro D, Ulian G, Valdrè G. Monte Carlo SEM-EDS micro- and nanoanalysis of ultrathin gold leaves in glass mosaic tesserae: Thickness effects and measurement strategy. Measurement: Journal of the International Measurement Confederation. 2018;129:211-7.
[18] Ritchie NWM. Spectrum Simulation in DTSA-II. Microscopy and Microanalysis. 2009;15:454-68.
[19] Jablonski A, Salvat F, Powell CJ. NIST electron elastic-scattering cross-section database. Gaithersburg, MD: National Institute of Standards and Technology; 2010.
[20] Czyzewski Z, Maccallum DO, Romig A, Joy DC. Calculations of Mott Scattering Cross-Section. Journal of Applied Physics. 1990;68:3066-72.
[21] Myklebust R, Newbury D, Yakowitz H. NBS Monte Carlo Electron Trajectory Calculation Program. In: Heinrich K, Yakowitz H, Newbury D, editors. NBS Special Publication. Washington, DC: National Bureau of Standards; 1976. p. 105.

[22] Joy DC, Luo S. An Empirical Stopping Power Relationship for Low-Energy Electrons. Scanning. 1989;11:176-80.
[23] Bethe HA, Ashkin J. Passage of radiation through matter. In: Segre E, editor. Experimental Nuclear Physics. New York, N.Y.: John Wiley & Sons; 1953.
[24] Bote D, Salvat F. Calculations of inner-shell ionization by electron impact with the distorted-wave and plane-wave Born approximations. Physical Review A. 2008;77.
[25] Bote D, Salvat F, Jablonski A, Powell CJ. Cross sections for ionization of K, L and M shells of atoms by impact of electrons and positrons with energies up to 1 GeV: Analytical formulas. Atomic Data and Nuclear Data Tables. 2009;95:871-909.
[26] Perkins ST, Cullen DE, Chen MH, Rathkopf J, Scofield J, Hubbell JH. Tables and graphs of atomic subshell and relaxation data derived from the LLNL Evaluated Atomic Data Library (EADL), Z = 1–100. Technical Report. Berkley, CA: Lawrence Livermore National Laboratory; 1991.
[27] Acosta E, Llovet X, Salvat F. Monte Carlo simulation of bremsstrahlung emission by electrons. Applied Physics Letters. 2002;80:3228-30.
[28] Salvat F, Fernandez-Varea JM, Sempau J. PENELOPE-2014: A code system for Monte Carlo simulation of electron and photon transport. Technical Report. Issy-les-Moulineaux, France: OECD/NEA Data Bank; 2015.
[29] Seltzer SM, Berger MJ. Bremsstrahlung spectra from electron interactions with screened atomic nuclei and orbital electrons. Nuclear Inst and Methods in Physics Research, B. 1985;12:95-134.
[30] Seltzer SM, Berger MJ. Bremsstrahlung energy spectra from electrons with kinetic energy 1 keV-10 GeV incident on screened nuclei and orbital electrons of neutral atoms with Z = 1-100. Atomic Data and Nuclear Data Tables. 1986;35:345-418.
[31] Chantler CT, Olsen K, Dragoset RA, Chang J, Kishore AR, Kotochigova SA, et al. NIST Standard Reference Database version 2.1. Available at http://physics.nist.gov/ffast: National Institute of Standards and Technology; 2005.
[32] Genée J, Berbenni S, Gey N, Lebensohn RA, Bonnet F. Particle interspacing effects on the mechanical behavior of a Fe–TiB2 metal matrix composite using FFT-based mesoscopic field dislocation mechanics. Advanced Modeling and Simulation in Engineering Sciences. 2020;7.
[33] Lartigue-Korinek S, Walls M, Haneche N, Cha L, Mazerolles L, Bonnet F. Interfaces and defects in a successfully hot-rolled steel-based composite Fe-TiB2. Acta Materialia. 2015;98:297-305.
[34] Munro RG. Material Properties of Titanium Diboride. Journal of Research of the National Institute of Standards and Technology. 2000;105:709-20.
[35] Rumble J. CRC Handbook of Chemistry and Physics. 100th ed. Florida, USA: CRC Press, Taylor & Francis, 2019.

[36] Ferreira JPJG, Branco FAB. The use of glass fiber-reinforced concrete as a structural material. Experimental Techniques. 2007;31:64-73.
[37] Yilmaz VT, Glasser FP. Reaction of alkali-resistant glass fibres with cement. Part 2. Durability in cement matrices conditioned with silica fume. Glass Technology. 1991;32:138-47.
[38] Butler M, Mechtcherine V, Hempel S. Experimental investigations on the durability of fibre-matrix interfaces in textile-reinforced concrete. Cement and Concrete Composites. 2009;31:221-31.
[39] Wang WC, Wang HY, Chang KH, Wang SY. Effect of high temperature on the strength and thermal conductivity of glass fiber concrete. Construction and Building Materials. 2020;245.
[40] Johnston CD. Fiber-reinforced cements and concrete. London and New York: Taylor & Francis, 2001.
[41] Gao SL, Mäder E, Abdkader A, Offermann P. Sizings on alkali-resistant glass fibers: Environmental effects on mechanical properties. Langmuir. 2003;19:2496-506.
[42] Scheffler C, Förster T, Mäder E, Heinrich G, Hempel S, Mechtcherine V. Aging of alkali-resistant glass and basalt fibers in alkaline solutions: Evaluation of the failure stress by Weibull distribution function. Journal of Non-Crystalline Solids. 2009;355:2588-95.
[43] ACI. Report on Fiber Reinforced Concrete, ACI 544.1R-96. American Concrete Institute; 2002.